UC Davis
UC Davis Previously Published Works

Title

Basal channels drive active surface hydrology and transverse ice shelf fracture

Permalink

https://escholarship.org/uc/item/4g657808

Journal

Science Advances, 4(6)

ISSN

2375-2548

Authors

Dow, Christine F
Lee, Won Sang
Greenbaum, Jamin S
et al.

Publication Date

2018-06-01

DOI

10.1126/sciadv.aao7212

Copyright Information

This work is made available under the terms of a Creative Commons Attribution-NonCommercial License, available at https://creativecommons.org/licenses/by-nc/4.0/

Peer reviewed

GEOLOGY

Basal channels drive active surface hydrology and transverse ice shelf fracture

Christine F. Dow[1]*, Won Sang Lee[2,3], Jamin S. Greenbaum[4], Chad A. Greene[4,5],
Donald D. Blankenship[4,5], Kristin Poinar[6]†, Alexander L. Forrest[7,8],
Duncan A. Young[4], Christopher J. Zappa[9]

Ice shelves control sea-level rise through frictional resistance, which slows the seaward flow of grounded glacial ice. Evidence from around Antarctica indicates that ice shelves are thinning and weakening, primarily driven by warm ocean water entering into the shelf cavities. We have identified a mechanism for ice shelf destabilization where basal channels underneath the shelves cause ice thinning that drives fracture perpendicular to flow. These channels also result in ice surface deformation, which diverts supraglacial rivers into the transverse fractures. We report direct evidence that a major 2016 calving event at Nansen Ice Shelf in the Ross Sea was the result of fracture driven by such channelized thinning and demonstrate that similar basal channel–driven transverse fractures occur elsewhere in Greenland and Antarctica. In the event of increased basal and surface melt resulting from rising ocean and air temperatures, ice shelves will become increasingly vulnerable to these tandem effects of basal channel destabilization.

INTRODUCTION

The buttressing effect of ice shelves is a primary control on the stability of vulnerable regions of the Antarctic (1, 2). Loss of ice shelf frictional resistance can accelerate grounded glacial ice into the ocean, which contributes to sea-level rise (3, 4). Basal channels, which have been identified under many Antarctic ice shelves (5), are known to thin the ice and alter the stress distribution, making the ice shelf more susceptible to basal or surface fractures (5–7). Flow-parallel fractures have been observed and attributed to these channels (5, 6), but flow-perpendicular fractures have instead been interpreted as a result of basal crevassing, not directly related to basal channels (8, 9). On the surface of ice shelves, river channels have been identified in satellite imagery. These rivers have been previously reported for Nansen Ice Shelf (10, 11), for Larsen B immediately before its collapse (12), and throughout East Antarctica (13–15); to date, these rivers have not been linked to the presence of basal channels.

We present evidence from multiple ice shelves in Antarctica and one in Greenland, which demonstrate that basal channels drive the formation of transverse surface fractures (Fig. 1). Basal channels in two of these systems also facilitate formation of a surface river, increasing the susceptibility of the ice shelf to localized thinning and rifting by hydrofracture.

RESULTS

Study site

Our main study area is the Nansen Ice Shelf, which is located in the western Ross Sea, adjacent to the Drygalski Ice Tongue in East Antarctica.

This shelf covers ~2000 km^2 and is 200 m thick toward its oceanic terminus. Ice flow on the shelf averages 150 m year^{-1} (16) and is primarily sourced from Reeves and Priestley glaciers (Fig. 2A). Once floating, these two ice bodies join to form a suture zone; the resulting differential shelf draft causes ocean water to rise and accelerate (17) with the enhanced melting forming a basal channel that persists for the length of the shelf, which we have identified using aerial geophysics methods.

In January 2014, a surface river was observed on Nansen Ice Shelf, cascading into a 200-m-wide, 20-km-long rift in the shelf (Fig. 2B) (10, 11). This 100-m-wide river was visible in satellite imagery (Fig. 2A) and formed 20 km downstream from the grounding line of Reeves Glacier. This river has previously been suggested to have a stabilizing effect on the Nansen Ice Shelf by removing water that might otherwise form into melt ponds (11). Here, we suggest that the location of the surface river is driven by the presence of the basal channel as, due to hydrostatic equilibrium, surface depressions in the ice shelf mirror areas with shallow basal drafts (Fig. 3, B to D) (6). In 2014, the river accumulated water along its 18-km length before plunging into the rift, 5 km from the calving front of Nansen Ice Shelf. In April 2016, a calving event occurred at this fracture, generating the 153-km^2 C-33 iceberg and a 61-km^2 unnamed iceberg (Fig. 2C).

The transverse fracture that culminated in this calving of two large icebergs was first visible in 1987 Landsat imagery with a width of <100 m and a length of 4 km (Fig. 4B). In 1987, the fracture was centered directly above the basal channel (Fig. 4B). Once formed, the fracture advected downstream and maintained a relatively constant geometry, confined to the region of thinner ice within the channel, until 2012, when it expanded from 4 to 13 km in length. Video footage of the 2014 Nansen River revealed ocean water refrozen in the fracture, indicating that full rifting had occurred. In situ data collected in November 2016, after the calving event, led to the identification of a new inland fracture on the ice shelf (Fig. 4B). The new fracture formed directly over the thinnest ice in the basal channel in a similar region to the 1987 fracture; this new fracture will likely seed a future calving event. We discuss the roles that both the basal channel and surface river likely played in the fracturing that led to the 2016 Nansen Ice Shelf calving event.
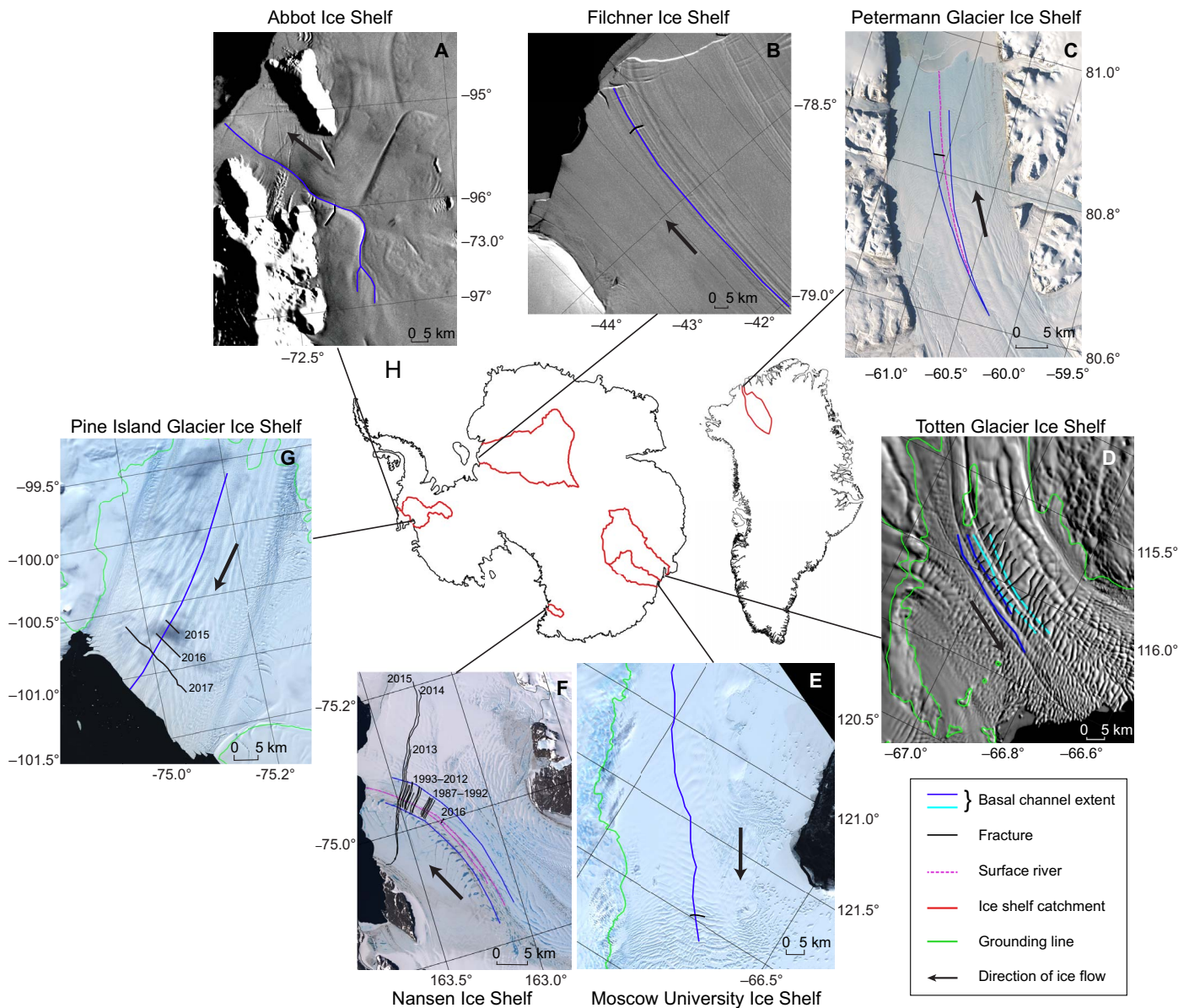
[1]Department of Geography and Environmental Management, University of Waterloo, 200 University Avenue West, Waterloo, Ontario N2L 3G1, Canada. [2]Unit of Ice Sheet and Sea Level Changes, Korea Polar Research Institute, Incheon, Republic of Korea. [3]Polar Sciences, Korea University of Science and Technology, Incheon, Republic of Korea. [4]Institute for Geophysics, Jackson School of Geosciences, University of Texas at Austin, Austin, TX 78758, USA. [5]Department of Geological Sciences, Jackson School of Geosciences, University of Texas at Austin, Austin, TX 78712, USA. [6]Crysopheric Sciences Laboratory, NASA Goddard Space Flight Center, Greenbelt, MD 20771, USA. [7]Civil and Environmental Engineering, University of California, Davis, One Shields Avenue, Davis, CA 95616, USA. [8]Tahoe Environmental Research Center, University of California, Davis, 291 Country Club Drive, Incline Village, NV 89451, USA. [9]Lamont-Doherty Earth Observatory, Columbia University, 61 Route 9W, Palisades, NY 10964, USA.
*Corresponding author. Email: christine.dow@uwaterloo.ca
†Present address: Department of Earth Science, University at Buffalo, Buffalo, NY 14260, USA.

Fig. 1. Transverse fractures related to ice shelf channels on Antarctic and Greenland ice shelves. In all images, transverse fractures are shown in black, basal channels are shown in blue, and black arrows indicate general ice-flow direction. (**A**) Image showing Abbot Ice Shelf from 2003 to 2004. (**B**) Moderate-resolution Imaging Spectroradiometer (MODIS) Mosaic of Antarctica (*41*) of Filchner Ice Shelf from 2003 to 2004. (**C**) Landsat image of Petermann Glacier Ice Shelf from 30 April 2017, with the fracture that appeared in 2016. The fracture is intersected by a surface river (pink) and is located directly above a basal channel, with the extent shown in blue, estimated from digital elevation model (DEM) calculations. (**D**) MODIS mosaic of Totten Glacier Ice Shelf from 2003 to 2004. The blue and cyan lines indicate the extent of two channels identified under Totten Glacier Ice Shelf from radar surveys with fractures that initiate from the center of the two basal channels. (**E**) Landsat image of Moscow University Ice Shelf from 9 November 2017. (**F**) Landsat image of Nansen Ice Shelf from 2 January 2014, with fracture extent from 1987 to 2015 in black as identified from Landsat imagery. A new fracture was identified in situ in 2016. Channel extent (blue) is estimated from radar surveys and DEM calculations. The surface river is shown in pink. (**G**) Landsat image of Pine Island Ice Shelf from 24 January 2017. A fracture initially appeared in Landsat imagery in 2015 and advected while expanding until the ice front calved along this rift in September 2017. (**H**) Location of the studied ice shelves in Antarctica and Greenland with the ice shelf catchment areas outlined in red.

Data acquisition

To investigate the characteristics of the Nansen Ice Shelf basal channel and its colocated surface river, we used airborne very high frequency ice-sounding radar and single-beam laser altimeter data collected by the International Collaborative Exploration of the Cryosphere through Aerogeophysical Profiling (ICECAP) project in October 2011 and the Geophysical Investigations of Marie Byrd Land Litho-

spheric Evolution (GIMBLE) project in December 2014. Each flight line intersected the surface river at a different point along its course (Fig. 2A). The surface altimetry and basal radar data from 2011 (Fig. 3B) and 2014 (Fig. 3, C and D) show the basal channel, the related surface depression, and the riverbed. These colocated surface and basal features are consistent both temporally and spatially and, in years with sufficient surface melt, manifest as one (or two parallel) surface rivers. In 2011,
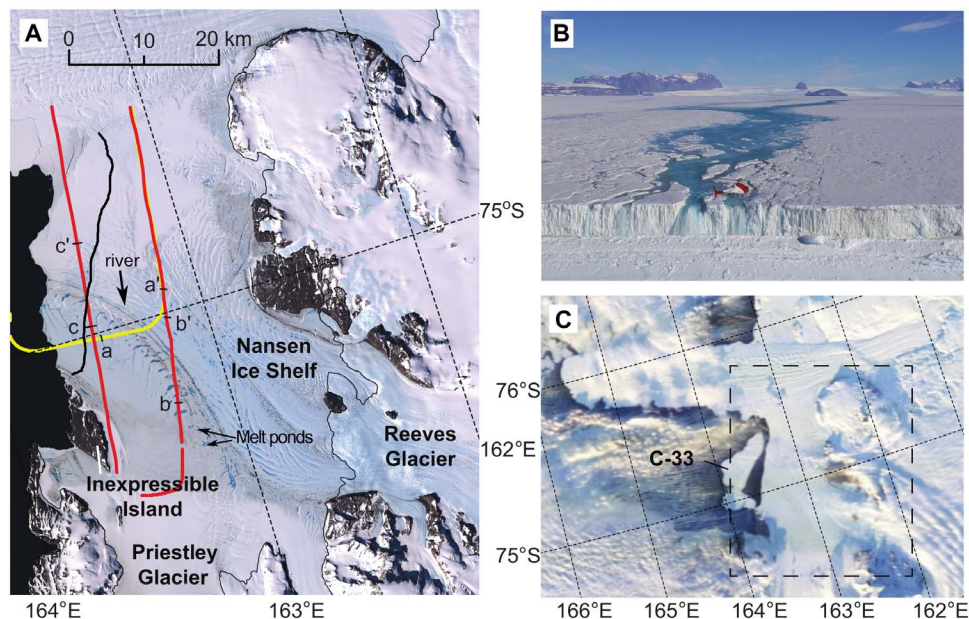
Fig. 2. Nansen Ice Shelf surface river and calving event. (**A**) Landsat image of the Nansen Ice Shelf region from 2 January 2014 overlain with aerogeophysical coverage from October 2011 (yellow) and December 2014 (red). The lowercase letters indicate the plotted extents of radar and altimetry data shown in Fig. 3 (B to D). The thick solid black line is the 2016 calving front, and the thin black line is the grounding line. (**B**) Nansen River on 13 January 2014 flowing into a transverse surface fracture. (**C**) MODIS image from 7 April 2016 showing the calving of two icebergs from the Nansen Ice Shelf along the fracture shown in (B). The dashed box indicates the spatial extent of (A).

the basal channel was on the order of 4 km wide and 70 m high. This cavity caused a hydrostatic depression of 10 m over the same region in the surface, which drew water from the surrounding regions on the ice shelf that, through thermal erosion, incised the surface a further 4 m to create two 100-m-wide rivers (Fig. 3B). In 2014, the flight line crossed the channel obliquely so that it appears wider (6 km); we calculate a flow-perpendicular width of 3.7 km (Fig. 3C). This flight line recrossed the channel over the rift in the ice shelf (data gap in Fig. 3D) where the width was 6 km (7 km in the oblique data). In both locations, the basal channel was 50 m high; its height and width are comparable to the central sub–ice shelf channels on Pine Island Glacier in West Antarctica (6).

DEM construction

We developed a DEM of the Nansen Ice Shelf surface to investigate the topography over a broader scale than the flight line observations allow. This DEM was constructed by combining radar and laser altimetry data with stereo photometry (Fig. 4A) (see Materials and Methods). Our DEM reveals that the surface depression visible in the radar transects spans the length of the ice shelf. We applied water flow routing algorithms to this DEM and found that, as observed in the Landsat imagery, meltwater from the Reeves and Priestley Glacier catchments converge into a surface river on the ice shelf (Fig. 4A). To estimate the basal topography of the ice shelf, we assumed hydrostatic equilibrium and inverted our surface DEM (see Materials and Methods). The basal DEM and the channel extents that we extracted from the radar data both indicate that the channel widens along flow (Fig. 4B), which could be due to higher melt rates near the ice shelf front or as a result of lateral stretching. Our basal DEM indicates that the basal channel initiates at the confluence of Reeves and Priestley glaciers as a result of this suture zone, which is consistent with theory and observations on other ice shelves (18, 19). Ice at the grounding line of Priestley Glacier is several hundred meters thicker than at Reeves (20); this thickness differential

will increase the advection speeds of warm, buoyant plumes, which should enhance basal melting in this region and induce a channel, as observed on the Amery Ice Shelf (19). The location of the channel along the suture zone suggests an origin primarily due to ocean melting (5, 17), rather than from subglacial water influx as seen at other Antarctic ice shelves (21).

DISCUSSION

Nansen Ice Shelf basal channel and fractures

The location of the 1987 fracture over the basal channel and the new fracture that was found in November 2016 in the same basal channel region both illustrate the weakening impact of the basal channel. To investigate the cause of these transverse fractures, we used ice shelf surface velocity products to calculate the surface strain rate field, as detailed in Materials and Methods. We anticipate fractures forming in areas where there is an increase in extensional strain rate. In the strain rate field calculated from MEaSUREs 1996–2016 average velocities (16), the greater principal strain rate was generally compressional in the area overlying part of the basal channel and extensional seaward of the 2016 fracture location (Fig. 5A). We also analyzed shorter-term strain rate fields using the Landsat8-derived Global Land Ice Velocity Extraction (GoLIVE) product (22). The GoLIVE data are generated only on water-free areas of the ice surface, limiting data coverage along the Nansen River channel during summer melt periods. As a result, we analyzed periods between October and November, before the surface melt season, from 2013 to 2016. All scenes that we analyzed featured bands of cross-flow compression and extension within the basal channel–induced surface depression (Fig. 5, B to E). The new 2016 fracture formed within the band of extension.

In both 2013 and 2014, the region where the fracture eventually formed experienced relatively small extensional strain rates in the transverse direction (Fig. 5, B and C). If the ice shelf was laterally spreading,
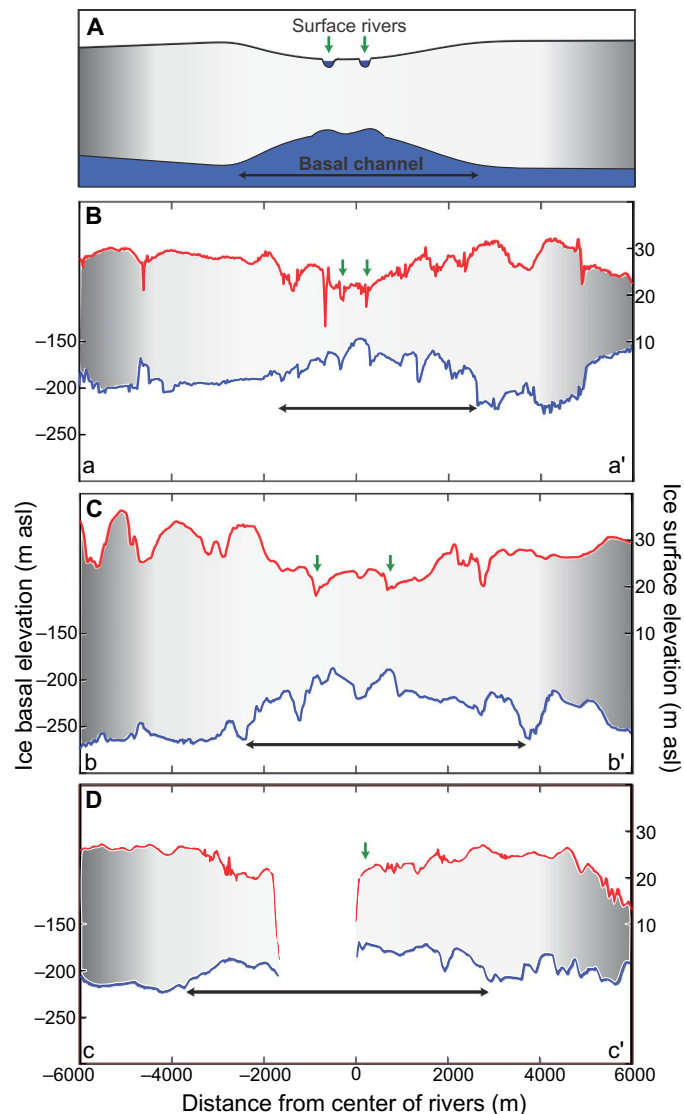
Fig. 3. Ice shelf surface and bed profiles. (**A**) Schematic of an ice shelf basal channel and a coincident ice surface depression that funnels meltwater, resulting in river formation and incision. The ice shelf is shown in gray. (**B** to **D**) Surface (red) and basal (blue) ice cross-sectional profiles from radar along the flight lines in Fig. 2A for (**B**) October 2011 and (**C** and **D**) December 2014. The green arrows indicate the location of the parallel surface rivers identified from Landsat imagery. The black arrows indicate the extent of the basal channel. The data gap in (**D**) is due to the ice shelf rift. m asl, meters above sea level.

causing higher extensional strain, a fracture could have formed in the thinnest ice along the length of the channel. However, as the Nansen Ice Shelf is laterally constrained, these transverse extensional strain rates were too small to allow fracture parallel to the ice flow direction.

In late 2015, the rate of extension increased and rotated to be extensive in the down-flow direction rather than in the cross-flow direction. This region of strong down-flow extension propagated back to (but not beyond) the location where the new fracture formed. A similar down-flow extensional pattern is seen in late 2016, just before identification of the fracture in the field (Fig. 5E). Using these data, we hypothesize that the release of friction due to the expansion (in 2015) and eventual cal-

ving (in 2016) of the 1987 fracture allowed flow acceleration, and therefore extensional strain, driving the formation of the new 2016 transverse fracture. This suggests that the longitudinal fracture location is controlled by the wider strain regime of the ice shelf, while its transverse location is fixed by the location of the basal channel.

Basal channel fractures in other ice shelves

We observe a similar basal channel–induced fracturing pattern on other ice shelves. A 2-km-wide transverse fracture appeared in 2016 on the ice shelf of Petermann Glacier, Greenland. Petermann Ice Shelf underwent two large calving events in 2010 and 2012 that originated from rifts propagating from the edge of the ice shelf (23). The 2016 fracture, however, was located in the center of the shelf directly overlying a basal channel, and was confined to the regions of the thinnest ice in the channel (Fig. 1C). This fracture intersected a surface river colocated with the basal channel, similar to the Nansen Ice Shelf. The Petermann Ice Shelf basal channel has high melt rates (24) and, combined with the potential for hydrofracture by the surface river, also demonstrates weakening of the shelf as illustrated by the latest fracture event.

Totten Glacier Ice Shelf hosts the highest density of basal channels identified around the Antarctic (5). The stability of the Totten Glacier Ice Shelf is of great concern because it provides a resistive force for grounded ice that could, in the event of ice shelf collapse, contribute at least 3.5 m to sea-level rise (25). We used ICECAP radar data to identify the extent of two of the Totten Ice Shelf basal channels. As on Petermann Ice Shelf, the thinnest region of the channel initiates transverse fractures that propagate laterally for multiple kilometers (Fig. 1D). Unlike Nansen and Petermann ice shelves, which each have one prominent fracture, Totten Ice Shelf has multiple fractures originating over the basal channels that propagate until they reach thicker ice. It is possible that these fractures originate as basal crevasses rather than surface crevasses but, similar to those on the other ice shelves that we discuss, they are limited to the thinnest ice associated with the basal channels. Once these fractures become unpinned from the grounded region flanking Totten Ice Shelf, they form the regions of active frontal calving.

Moscow University Ice Shelf is a region, like Totten Glacier Ice Shelf, where high melt rates occur over the grounding line (26). The basal channel that can be identified in MODIS imagery runs from the grounding line for 105 km along the full length of the ice shelf (5). A transverse fracture over the basal channel is visible in Landsat imagery from November 2017 with a length of 4.6 km (Fig. 1E).

Pine Island Glacier is one of the most vulnerable regions of the Antarctic to ice shelf collapse and has seen marked thinning rates and grounding line retreat over the last decade (4, 6). Pine Island Glacier Ice Shelf has had five large calving events between 2000 and 2017. The fracture that grew to cause the most recent calving event in September 2017 initiated over one of the ice shelf basal channels. The channels have been identified from MODIS imagery (5) and radar surveys (6). A 4-km-wide polynya identified from Landsat imagery in 2000 also supports the presence of a channel in this location. The fracture (Fig. 1G) can first be seen in March 2015 with a length of 3.7 km. By February, the fracture had moved 3.4 km downstream and lengthened to 7 km. In January 2017, the fracture was 5.4 km downstream and 19 km long. This fracture culminated in a calving event in September 2017 creating the 185-km^2 B-44 iceberg. The formation of a fracture originating from the center of the ice shelf and propagating laterally, rather than from the edge toward the center has previously been attributed to crevasses originating from the grounding line (27). Here, we suggest that thinning within the basal channel is a driver for the initial
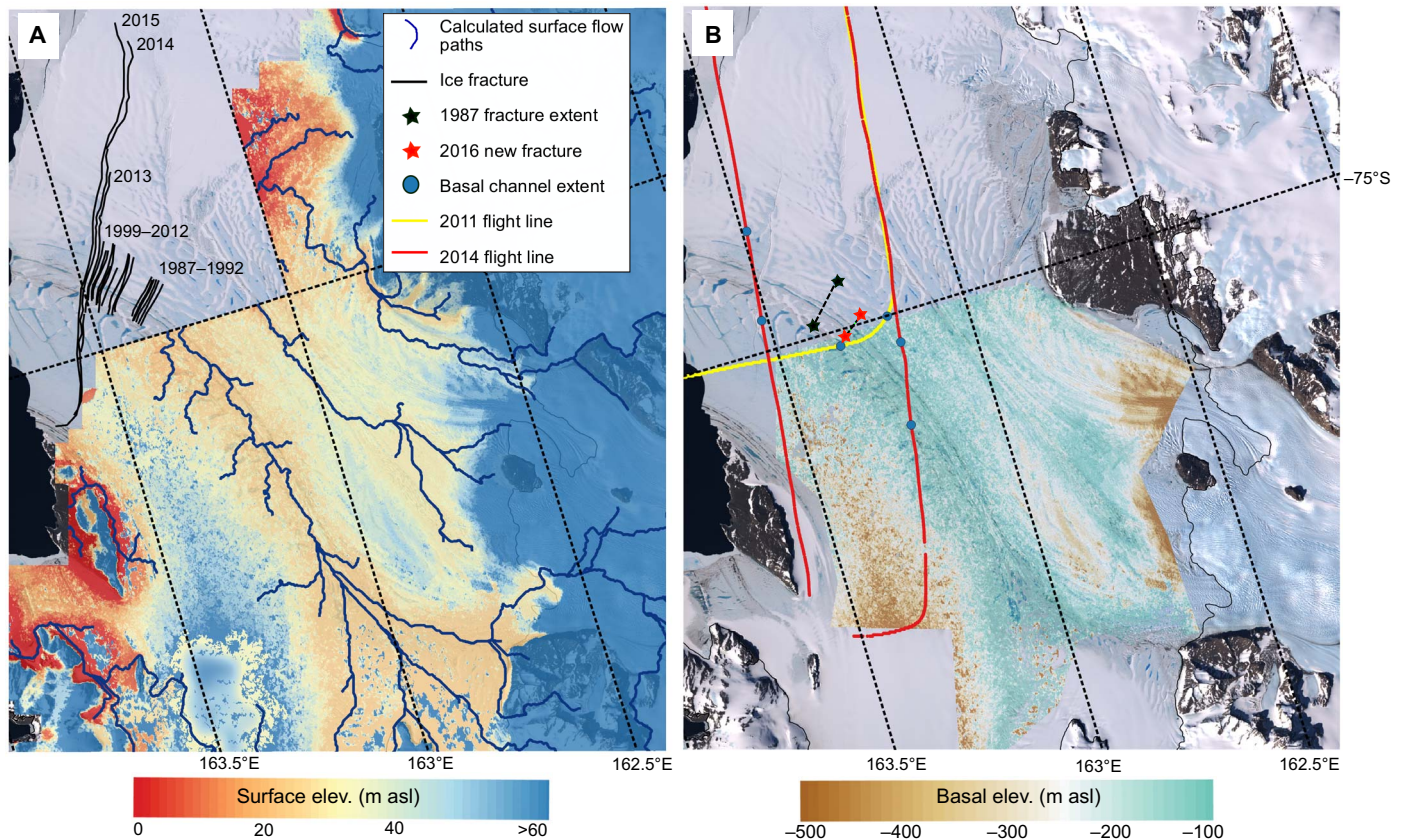
Fig. 4. Nansen ice surface and bed DEMs. (**A**) Surface DEM of Nansen Ice Shelf overlain on a Landsat image from 2 January 2014. Surface river routing in blue, calculated from the DEM, suggests that the Nansen River sources from both Reeves and Priestley glaciers. Fracture extent from 1987 to 2015, estimated from Landsat imagery, is shown in black and is consistent with the width of the basal channel until 2012–2013, when it expands suddenly. (**B**) Elevation of the ice shelf base was calculated assuming hydrostatic equilibrium. Yellow and red lines show flights from 2011 and 2014, respectively, with the blue points indicating the extent of the basal channels identified from the radar returns. Red stars and dashed line show the location of the new fracture identified during fieldwork in November 2016. Black stars and dashed line show the location of the initial fracture from 29 December 1987 Landsat imagery that ultimately caused the 2016 calving event.

transverse location of the fracture, and the role of grounding line–originated crevasses is to determine the longitudinal location of fracture formation.

Abbot Ice Shelf, in West Antarctica, lies adjacent to Pine Island Glacier Ice Shelf and is a region where basal melt has been the primary mechanism of mass loss rather than calving (*26*), although the mass loss rates of this ice shelf are low compared to other ice shelves in the area because of the shallow draft compared to the depth of warm ocean water (*4*). Sufficient melt occurs, however, to cause an ocean-sourced basal channel with a length of 135 km (*5*). A 7.6-km-long transverse fracture initiates from the center of the basal channel and propagates laterally, similar to that seen on Petermann Ice Shelf (Fig. 1A). A second possible fracture initiates from the basal channel in the opposite direction, 17 km oceanward of the first fracture.

In contrast to Abbot Ice Shelf, mass loss at Filchner Ice Shelf is dominated by calving mechanisms (*26*). At Filcher Ice Shelf, two basal channels have been identified that have subglacial sources (*5*). One of these channels originates from the grounding line of Recovery Glacier, which drains 8% of the East Antarctic's ice volume. This basal channel runs 340 km along the length of Filchner Ice Shelf. A transverse fracture is visible above the width of this basal channel, stretching to a length of 6 km, within 17 km of the ice front (Fig. 1B).

The role of basal channels in ice fracture
The formation of transverse fractures over thin ice caused by basal channels appears to be a phenomenon observed across ice shelves with variable characteristics, including highly sensitive systems. Many of these systems have basal channels that do not yet have surface rivers associated with them, suggesting that the thinning by the basal channel plays the primary role for fracturing. At the Nansen Ice Shelf, we have evidence of this channel-induced fracturing leading to a large calving event and subsequent refracturing over the basal channel. The Nansen case study, along with the multiple examples of basal channel–induced fracturing, demonstrates the vulnerability of ice shelves to channel-induced calving. This phenomenon is likely to become more prevalent with increased access of warm ocean water to ice shelves exacerbating basal channel melting and warming air temperatures enhancing surface water formation. Such fracture-driven calving, controlled by the ice thinning in the basal channel and the ice shelf strain regime, could breach the compressive arch found where ice shelves unpin from bounding regions (*28*) resulting in ice shelf collapse.

The role of surface hydrology in ice fracture
Surface rivers are not identified over all the basal channels that have transverse fractures and can therefore not be the leading cause for fracture
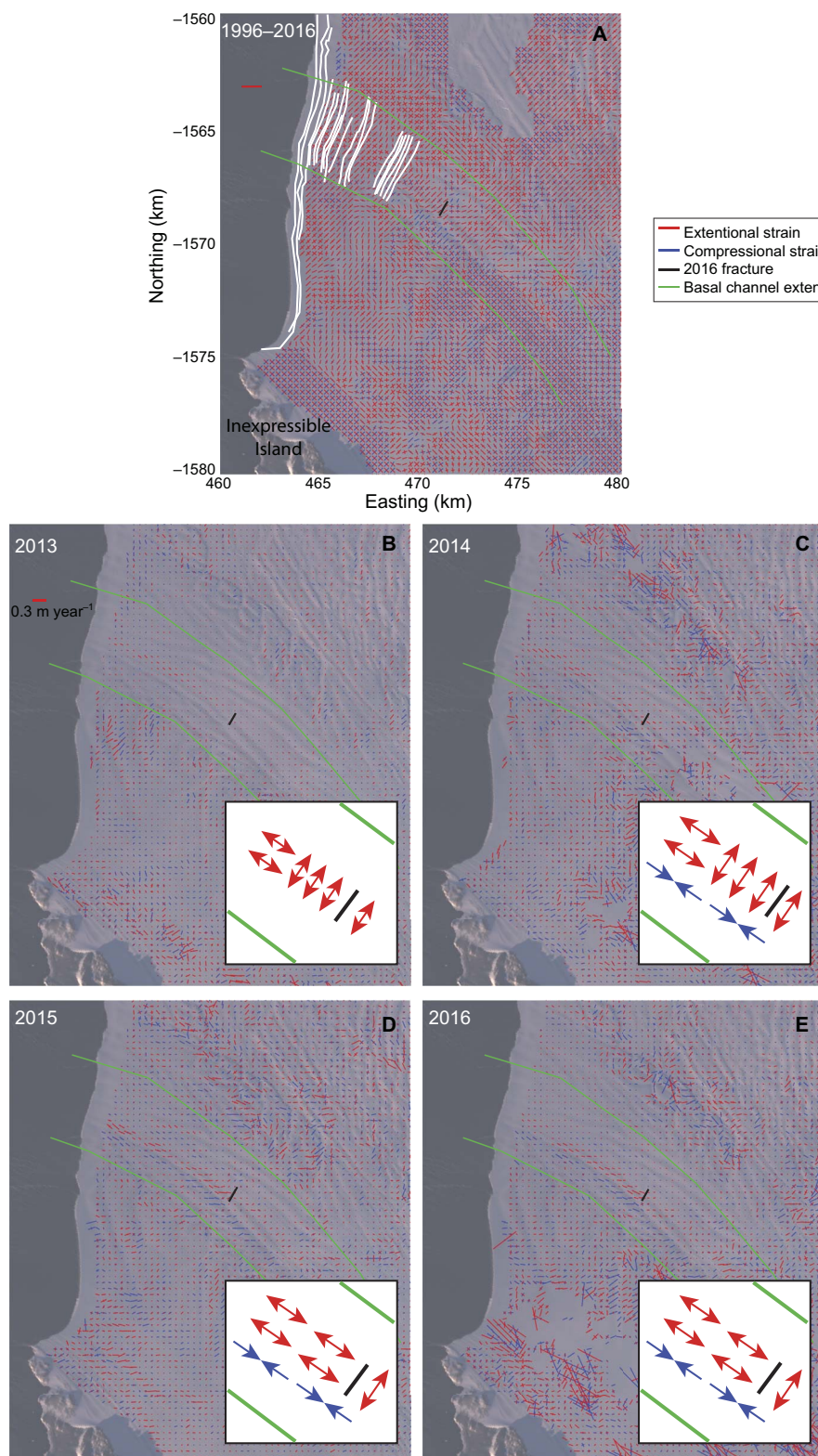
Fig. 5. Principal strain rate axes for Nansen Ice Shelf. Magnitude and orientation of the principal strain rates are shown by the blue (compressional) and red (extensional) lines. The black line shows the location of the new 2016 fracture. The green lines show the extent of the basal channel. The fields are overlain on a Landsat image from 22 March 2017. Insets show a schematic of the general extensional and compressional strain rate orientations for the largest principal strain rates in the region of the 2016 fracture. (**A**) Strain rate axes calculated from the 1996–2016 average MeaSUREs velocity data set (*16*). The white lines show the position and length evolution of the fracture initially identified in 1987. (**B** to **E**) Strain rates from Landsat GoLIVE velocity products spanning (B) 8 November to 10 December 2013, (C) 15 September to 17 October 2014, (D) 13 October to 14 November 2015, and (E) 29 September to 31 October 2016.

initialization. However, the addition of a surface river on ice thinned by basal channels could cause further weakening by surface incision (8) and hydrofracturing (9) when flowing into basal channel–driven fractures, if the latter do not initially form as full-thickness rifts.

It has been suggested that surface rivers may stabilize ice shelves by removing water that might otherwise collect into melt ponds (11). However, we demonstrate that the Nansen surface rivers only remove water from the region of the ice shelf where the basal channel causes a surface depression (Fig. 4A). The river can then enhance ice shelf surface erosion in the thinnest ice overlying a basal channel and will focus water into transverse surface fractures more rapidly than would be possible for water separated into multiple melt pond drainage basins. Although the catastrophic collapse of the Larsen B Ice Shelf was primarily associated with melt ponds (29), mapping of surface water features leading up to the shelf disintegration event also identified surface rivers, which ultimately did not inhibit large-scale melt pond–related fracturing (12). Surface ponds also form on Nansen Ice Shelf (Fig. 2A); however, we have shown that transverse fracturing on this (and other) ice shelves is controlled by basal channel processes. If the surface rivers do not cause weakening of an ice shelf by incision or hydrofracture, at the very least they, through hydrostatic balance with basal channels, are indicators of their presence, which, as we have demonstrated, are locations of potential weakness in ice shelves. Our evidence therefore suggests that the presence of coincident surface rivers and basal channels does not stabilize the ice shelf.

Synthesis and implications for ice shelf stability

A large number of ice shelf basal channels are present around Antarctica (5), and increased access of warm ocean water is expected to be a key driver for enlarging basal channels and weakening ice shelves in the future (30). Our study provides direct evidence for the weakening impact of basal channels in the present day due to the formation of transverse fractures. Previously, fractures parallel to flow have been attributed to basal channel processes (6), but our new evidence showing transverse fractures and their direct link to ice shelf calving indicates the important role of basal channel thinning in the future stability of ice shelves. With rising air and ocean temperatures, the processes reported here may become prevalent elsewhere in Antarctica. As a result, the role of transverse fracturing driven by basal channels should be included in models projecting future Antarctic ice sheet mass balance.

MATERIALS AND METHODS
Radar surface and bed elevation
The ice surface and basal elevations for all profiles in Fig. 4 were derived using the High Capability Airborne Radar Sounder (HiCARS) that was used on the ICECAP platform in 2011 and the GIMBLE platform in 2014. This system was also used to identify the extent of basal channels in Fig. 1B. Ice surface and basal elevations were extracted using a common semiautomatic method with rough localization from manual picking. A detailed description of the HiCARS system, processing techniques, and measurement uncertainties can be found in the literature (31). The vertical resolution of the radar data is related to the signal source wavelet, the receiver bandwidth, the sampling rate, the processing applied, and the medium through which the signal transmits; HiCARS has a fundamental vertical resolution of ~10 m in air and ~5.6 m in ice.

Generation of Nansen Ice Shelf surface DEM
The 50-m resolution surface DEM used in this study was generated by combining a 1-km gridded elevation data set [BDEM (32)], the ASTER

GDEM2 (Advanced Spaceborne Thermal Emission and Reflection Radiometer Global Digital Elevation Model), and more than 90,000 laser altimetry measurements from ICESat (Ice, Cloud, and Land Elevation Satellite) (33), IceBridge ATM (Airborne Topographic Mapper) (34), and IceBridge Riegl (35). Our custom DEM blends the high precision of ASTER GDEM2 for short-wavelength topographic features with the superior accuracy of BDEM for large-scale features (fig. S1).

We developed a custom surface DEM for this work because all readily available surface DEMs failed to sufficiently replicate the patterns of supraglacial water flow observed on the Nansen Ice Shelf. We compared several publicly available DEMs to satellite and airborne laser altimetry using the data interpolation functions in Antarctic Mapping Tools for MATLAB (36). We found that BDEM exhibited the best fit ($z_{laser} − z_{DEM} = 0.5 \pm 3.7$ m) with more than 15,000 laser altimetry measurements taken over the ice shelf, while ASTER GDEM2 showed the poorest fit to data ($z_{laser} − z_{DEM} = 10.3 \pm 51.4$ m). We also assessed the DEMs by comparing the surface water routing, calculated with TopoToolbox 2 (37) for each DEM, to observations. Each of the 1-km DEMs allowed formation of a surface river in the rough proximity of the river observed in 2014. The finer-resolution ASTER GDEM2, however, produced nonphysical flow patterns such as landward-flowing rivers. Figure S1 shows the absolute error ($z_{laser} − z_{DEM}$) and the predicted surface water routing patterns for BDEM, ASTER GDEM2, and our custom DEM.

We used the BDEM as the basis for the large-scale topography of the custom surface DEM. In an effort to correct errors in BDEM introduced by the steep topography that bounds Nansen Ice Shelf (where radar altimetry tends to perform poorly) and uncertainties in the firn depth, we adjusted the BDEM using all available laser altimetry in the region. We discarded ICESat measurements with any quality flags or gain values exceeding 30. We also include airborne laser altimetry from the IceBridge Riegl and ATM sensors. We used the Antarctic Mapping Tools iceflex_interp function to calculate a coefficient of flexure for all laser altimetry measurements. We next corrected for tides using CATS2008b (38) and inverse barometer effects (39) using ECMWF (European Centre for Medium-Range Weather Forecasts) ERA-Interim surface pressure reanalysis data. Corrections applied to floating ice measurements were small and contributed very little to the final DEM, but we included them as proper treatment of the data.

We fitted a surface to the differences between the laser measurements and interpolated BDEM elevations, added that surface to the BDEM, resampled to 50-m resolution, and referenced the resulting surface to the geoid. Adjustments to the BDEM were minor (<4 m) within the watershed of the observed surface river but reached 20 m in a small area near the north end of Nansen Ice Shelf.

Although we found inaccuracies in the ASTER GDEM2 over large scales, we incorporated its short-wavelength features in our custom DEM to take advantage of photogrammetry's unparalleled small-scale precision. We applied a 3 × 3 median filter to the ASTER GDEM2 to reduce speckle and to serve as an anti-aliasing mechanism, then we interpolated it to our 50-m grid. After interpolation, we filled large areas of missing data with values from the adjusted BDEM and smoothed any seams by interpolating between the two data sets along a 500-m border where they join. We did not attempt to model the surface where the ASTER GDEM2 is missing a large section of data near the northern edge of the Nansen Ice Shelf. ASTER GDEM2 contains an area of noise and missing data likely due to the presence of windblown-drifted snow (74.8°S, 163.5°E), but this region had negligible effects on our final water routing predictions.

Finally, we completed our custom DEM by summing the filled ASTER GDEM2 and the Gaussian low-pass–filtered adjusted BDEM, then

subtracting the Gaussian low-pass–filtered filled ASTER GDEM2. The final product contains long-wavelength features from the adjusted BDEM and short-wavelength features from the filled ASTER GDEM2. By this method, $2\pi\sigma$, where σ is the standard deviation of the Gaussian filter, represents the crossover wavelength at which the adjusted BDEM and the filled ASTER GDEM2 contribute equally to our custom DEM.

We determined the optimum crossover wavelength, and therefore the σ for use in the Gaussian filter, by applying TopoToolbox 2 to predict flow paths for water at the headwaters of the surface river observed in 2014. We performed this analysis for DEMs that we generated using multiple values of σ. We converted the resulting flow paths to a curvilinear coordinate system, which we defined from manual picks for the river centerline as seen consistently in Landsat imagery. We found that an effective crossover wavelength of 4250 m reproduced the river flow path with the lowest root mean square (RMS) error, 347 m, compared to the observed river flow path. It should be noted that the river flow path is relatively insensitive to the choice of crossover wavelength: It reproduced within 1-km RMS error whether the adjusted BDEM was used alone or if it was blended with the filled ASTER GDEM2 up to a crossover wavelength of 12 km. The robustness of the river feature implies that it is driven by underlying large-scale topographic phenomena.

Generation of Nansen Ice Shelf basal DEM

We used our custom surface DEM for hydrostatic calculations to estimate the ice thickness and basal elevation of Nansen Ice Shelf. Calculation of the hydrostatic thickness assumes that the ice shelf is fully floating and in hydrostatic balance. We calculated the ice thickness (H) as

$$H = \frac{\rho_w Z_s}{\rho_w - \rho_i}$$

where Z_s is the ice shelf surface elevation (m asl), ρ_w is the density of seawater (1027 kg m^{-3}), and ρ_i is the density of ice (900 kg m^{-3}). This formulation assumes that there is no firn, which is reasonable because strong katabatic winds from Reeves and Priestley glaciers expose blue ice over much of the Nansen Ice Shelf surface.

Strain rate calculations

We used velocities from MEaSUREs interferometric synthetic aperture radar (InSAR)–derived Antarctic ice velocity data (16) and the Landsat8-derived GoLIVE product (22) to calculate strain rates on Nansen Ice Shelf. The former are an average of velocities between 1996 and 2016, and the latter are snapshots of velocity between 2013 and 2017. We analyzed four GoLIVE velocity data sets between 2013 and 2016 with 32-day separation in the period of October to November to avoid noise produced by surface meltwater on the ice shelf. The four GoLIVE scenes were selected to optimize both data coverage and year-to-year temporal overlap with one another, in an effort to aid qualitative comparison of the strain rate fields.

The MEaSUREs and GoLIVE products are produced on horizontal x-y grids that do not necessarily align with the flow of ice bodies. As a result, we used the MEaSUREs velocity data to establish the average flow direction of Nansen Ice Shelf and rotated to a local coordinate system accordingly. In our application, x is therefore the horizontal down-flow direction and y is the across-flow direction. We interpolated the MEaSUREs data onto the same 300×300 m grid for data comparison purposes. We calculated the magnitudes of the principal strain rates as

$$\dot{\epsilon}_1 = \frac{1}{2}\left[\frac{\partial u}{\partial x} + \frac{\partial v}{\partial y}\right] - \sqrt{\frac{1}{4}\left[\frac{\partial u}{\partial x} - \frac{\partial v}{\partial y}\right] + \frac{1}{2}\left[\frac{\partial u}{\partial y} + \frac{\partial v}{\partial x}\right]}$$

$$\dot{\epsilon}_3 = \frac{1}{2}\left[\frac{\partial u}{\partial x} + \frac{\partial v}{\partial y}\right] + \sqrt{\frac{1}{4}\left[\frac{\partial u}{\partial x} - \frac{\partial v}{\partial y}\right] + \frac{1}{2}\left[\frac{\partial u}{\partial y} + \frac{\partial v}{\partial x}\right]}$$

where u and v are the velocity in the local coordinate system x and y directions, respectively. We applied centered differencing over two grid cells, which in our local coordinate system results in the strain rates averaged over 420 m, or approximately 1 to 2 ice thicknesses. The directions of the principal strain axes are calculated as

$$\theta = \arctan\left(\frac{2\dot{\epsilon}_{xy}}{\dot{\epsilon}_x - \dot{\epsilon}_y}\right)\frac{1}{2}$$

where

$$\dot{\epsilon}_x = \frac{\partial u}{\partial x}$$

$$\dot{\epsilon}_y = \frac{\partial v}{\partial y}$$

$$\dot{\epsilon}_{xy} = \left(\frac{1}{2}\left[\frac{\partial u}{\partial y} + \frac{\partial v}{\partial x}\right]\right)$$

Using these equations, we obtained the magnitude and direction of the most extensive principal strain rate $\dot{\epsilon}_3$, and least extensive principal strain rate $\dot{\epsilon}_1$. The direction, θ, gives the angle between the y axis and $\dot{\epsilon}_1$, if $\dot{\epsilon}_x > \dot{\epsilon}_y$, and between the y axis and $\dot{\epsilon}_3$ otherwise (40). Positive strain rates reflect extensional conditions, and negative strain rates represent compressional conditions on the ice shelf surface.

REFERENCES AND NOTES

1. T. K. Dupont, R. B. Alley, Assessment of the importance of ice-shelf buttressing to ice-sheet flow. *Geophys. Res. Lett.* **32**, L04503 (2005).
2. G. H. Gudmundsson, Ice-shelf buttressing and the stability of marine ice sheets. *Cryosphere* **7**, 647–655 (2013).
3. T. A. Scambos, J. A. Bohlander, C. A. Shuman, P. Skvarca, Glacier acceleration and thinning after ice shelf collapse in the Larsen B embayment, Antarctica. *Geophys. Res. Lett.* **31**, L18402 (2004).
4. H. D. Pritchard, S. R. M. Ligtenberg, H. A. Fricker, D. G. Vaughan, M. R. van den Broeke, L. Padman, Antarctic ice-sheet loss driven by basal melting of ice shelves. *Nature* **484**, 502–505 (2012).
5. K. E. Alley, T. A. Scambos, M. R. Siegfried, H. A. Fricker, Impacts of warm water on Antarctic ice shelf stability through basal channel formation. *Nat. Geosci.* **9**, 290–293 (2016).
6. D. G. Vaughan, H. F. J. Corr, R. A. Bindschadler, P. Dutrieux, G. H. Gudmundsson, A. Jenkins, T. Newman, P. Vornberger, D. J. Wingham, Subglacial melt channels and fracture in the floating part of Pine Island Glacier, Antarctica. *J. Geophys. Res.* **117**, F03012 (2012).
7. B. Kulessa, D. Jansen, A. J. Luckman, E. C. King, P. R. Sammonds, Marine ice regulates the future stability of a large Antarctic ice shelf. *Nat. Commun.* **5**, 3707 (2014).
8. J. N. Bassis, Y Ma, Evolution of basal crevasses links ice shelf stability to ocean forcing. *Earth Planet. Sci. Lett.* **409**, 203–211 (2015).

9. D. McGrath, K. Steffen, H. Rajaram, T. Scambos, W. Abdalati, E. Rignot, Basal crevasses on the Larsen C Ice Shelf, Antarctica: Implications for meltwater ponding and hydrofracture. *Geophys. Res. Lett.* **39**, L16504 (2012).

10. M. Moctezuma-Flores, F. Parmiggiani, SAR observations of the Nansen Ice Shelf fracture. *Eur. Phys. J. Plus* **131**, 384 (2016).

11. R. E. Bell, W. Chu, J. Kingslake, I. Das, M. Tedesco, K. J. Tinto, C. J. Zappa, M. Frezzotti, A. Boghosian, W. S. Lee, Antarctic ice shelf potentially stabilized by export of meltwater in surface river. *Nature* **544**, 344–348 (2017).

12. N. F. Glasser, T. A. Scambos, A structural glaciological analysis of the 2002 Larsen B ice-shelf collapse. *J. Glaciol.* **54**, 3–16 (2008).

13. M. Mellor, G. McKinnon, The Amery Ice Shelf and its hinterland. *Polar Rec.* **10**, 30–34 (1960).

14. H. A. Phillips, Surface meltstreams on the Amery Ice Shelf, East Antarctica. *Ann. Glaciol.* **27**, 177–181 (1998).

15. J. Kingslake, J. C. Ely, I. Das, R. E. Bell, Widespread movement of meltwater onto and across Antarctic ice shelves. *Nature* **544**, 349–352 (2017).

16. E. Rignot, J. Mouginot, B. Scheuchl, Ice flow of the Antarctic ice sheet. *Science* **333**, 1427–1430 (2011).

17. C. V. Gladish, D. M. Holland, P. R. Holland, S. F. Price, Ice-shelf basal channels in a coupled ice/ocean model. *J. Glaciol.* **58**, 1227–1244 (2012).

18. O. V. Sergienko, Basal channels on ice shelves. *J. Geophys. Res. Earth Surf.* **118**, 1342–1355 (2013).

19. H. A. Fricker, R. Coleman, L. Padman, T. A. Scambos, J. Bohlander, K. M. Brunt, Mapping the grounding zone of the Amery Ice Shelf, East Antarctica using InSAR, MODIS and ICESat. *Antarct. Sci.* **21**, 515–532 (2009).

20. M. Frezzotti, I. E. Tabacco, A. Zirizzotti, Ice discharge of eastern Dome C drainage area, Antarctica, determined from airborne radar survey and satellite image analysis. *J. Glaciol.* **46**, 253–264 (2000).

21. A. M. Le Brocq, N. Ross, J. A. Griggs, R. G. Bingham, H. F. J. Corr, F. Ferraccioli, A. Jenkins, T. A. Jordan, A. J. Payne, D. M. Rippin, M. J. Siegert, Evidence from ice shelves for channelized meltwater flow beneath the Antarctic Ice Sheet. *Nat. Geosci.* **6**, 945–948 (2013).

22. M. Fahnestock, T. Scambos, T. Moon, A. Gardner, T. Haran, M. Klinger, Rapid large-area mapping of ice flow using Landsat 8. *Remote Sens. Environ.* **185**, 84–94 (2016).

23. A. Münchow, L. Padman, H. A. Fricker, Interannual changes of the floating ice shelf of Petermann Gletscher, North Greenland, from 2000 to 2012. *J. Glaciol.* **60**, 489–499 (2014).

24. E. Rignot, K. Steffen, Channelized bottom melting and stability of floating ice shelves. *Geophys. Res. Lett.* **35**, L02503 (2008).

25. J. S. Greenbaum, D. D. Blankenship, D. A. Young, T. G. Richter, J. L. Roberts, A. R. A. Aitken, B. Legresy, D. M. Schroeder, R. C. Warner, T. D. van Ommen, M. J. Siegert, Ocean access to a cavity beneath Totten Glacier in East Antarctica. *Nat. Geosci.* **8**, 294–298 (2015).

26. E. Rignot, S. Jacobs, J. Mouginot, B. Scheuchl, Ice-shelf melting around Antarctica. *Science* **341**, 266–270 (2013).

27. S. Jeong, I. M. Howat, J. N. Bassis, Accelerated ice shelf rifting and retreat at Pine Island Glacier, West Antarctica. *Geophys. Res. Lett.* **43**, 11720–11725 (2016).

28. D. Jansen, A. J. Luckman, A. Cook, S. Bevan, B. Kulessa, B. Hubbard, P. R. Holland, Brief communication: Newly developing rift in Larsen C Ice Shelf presents significant risk to stability. *Cryosphere* **9**, 1223–1227 (2015).

29. A. Luckman, A. Elvidge, D. Jansen, B. Kulessa, P. K. Munneke, J. King, N. E. Barrand, Surface melt and ponding on Larsen C Ice Shelf and the impact of föhn winds. *Antarct. Sci.* **26**, 625–635 (2014).

30. S. S. Jacobs, A. Jenkins, C. F. Giulivi, P. Dutrieux, Stronger ocean circulation and increased melting under Pine Island Glacier ice shelf. *Nat. Geosci.* **4**, 519–523 (2011).

31. M. E. Peters, D. D. Blankenship, S. P. Carter, S. D. Kempf, D. A. Young, J. W. Holt, Along-track focusing of airborne radar sounding data from West Antarctica for improving basal reflection analysis and layer detection. *IEEE Trans. Geosci. Remote Sens.* **45**, 2725–2736 (2007).

32. J. L. Bamber, J. L. Gomez-Dans, J. A. Griggs, A new 1 km digital elevation model of the Antarctic derived from combined satellite radar and laser data – Part 1: Data and methods. *Cryosphere* **3**, 101–111 (2009).

33. H. J. Zwally, R. Schutz, C. Bentley, J. Bufton, T. Herring, J. Minster, J. Spinhirne, R. Thomas, *GLAS/ICESat L2 Antarctic and Greenland Ice Sheet Altimetry Data, Version 34* (GLAH12) (NASA National Snow and Ice Data Center Distributed Archive Active Center, Boulder, CO, 2012).

34. W. B. Krabill, *IceBridge ATM L1B Elevation and Return Strength, Version 2* (ILATM2) (NASA National Snow and Ice Data Center Distributed Active Archive Center, Boulder, CO, 2016).

35. D. D. Blankenship, S. D. Kempf, D. A. Young, J. L. Roberts, T. van Ommen, R. Forsberg, M. J. Siegert, S. J. Palmer, J. A. Dowdeswell, *IceBridge Riegl Laser Altimeter L2 Geolocated Surface Elevation Triplets, Version 1* (ILUTP2) (NASA National Snow and Ice Data Center Distributed Active Archive Center, Boulder, CO, 2013).

36. C. A. Greene, D. E. Gwyther, D. D. Blankenship, Antarctic Mapping Tools for MATLAB. *Comput. Geosci.* **104**, 151–157 (2017).

37. W. Schwanghart, D. Scherler, Short Communication: TopoToolbox 2 – MATLAB-based software for topographic analysis and modeling in Earth surface sciences. *Earth Surf. Dyn.* **2**, 1–7 (2014).

38. L. Padman, H. A. Fricker, R. Coleman, S. Howard, L. Erofeeva, A new tide model for the Antarctic ice shelves and seas. *Ann. Glaciol.* **34**, 247–254 (2002).

39. L. Padman, M. King, D. Goring, H. Corr, R. Coleman, Ice-shelf elevation changes due to atmospheric pressure variations. *J. Glaciol.* **49**, 521–526 (2003).

40. J. T. Harper, N. F. Humphrey, W. T. Pfeffer, Crevasse patterns and the strain-rate tensor: A high-resolution comparison. *J. Glaciol.* **44**, 68–76 (1998).

41. T. A. Scambos, T. M. Haran, M. A. Fahnestock, T. H. Painter, J. Bohlander, MODIS-based Mosaic of Antarctica (MOA) data sets: Continent-wide surface morphology and snow grain size. *Remote Sens. Environ.* **111**, 242–257 (2007).